LASER ASSISTED CHEMICAL BATH GROWTH TECHNIQUE OF ZINC OXIDE COMPOSITE FOR ENHANCED UV PHOTODETECTOR PERFORMANCE

SAMER HUSNI ABDEL RAZZAQ ZYOUD

UNIVERSITI SAINS MALAYSIA

2025

LASER ASSISTED CHEMICAL BATH GROWTH TECHNIQUE OF ZINC OXIDE COMPOSITE FOR ENHANCED UV PHOTODETECTOR PERFORMANCE

by

SAMER HUSNI ABDEL RAZZAQ ZYOUD

Thesis submitted in fulfilment of the requirements
for the degree of
Doctor of Philosophy

September 2025

ACKNOWLEDGEMENTS

Alhamdulillah, with a heart overflowing with gratitude, I humbly extend my deepest thanks to Allah SWT, whose boundless mercy and guidance have been my constant companions on this demanding yet fulfilling journey. I have reached this significant milestone in my academic journey through His grace. To my esteemed supervisor, PROFESSOR MADYA DR. AHMAD FAIRUZ BIN OMAR, words fall short of expressing my appreciation. Your wisdom, patience, and unwavering support have guided me through the difficulties of my research and have also been a beacon of hope in moments of doubt and challenge. The love and support of my beloved wife, BATOOL, have been the bedrock upon which I built my academic aspirations. Her patience, love, and unwavering faith in me have been my sanctuary, making the challenges of this journey manageable. To my daughters, SALINA, SANDRA, and SANDY – your cheerfulness and encouragement have brought light into my days of toil. My family, my dear mother, siblings, and my late father – you are the unsung heroes of my story. Your unconditional love, sacrifices, and endless prayers have been the wind beneath my wings. To my late father, I pray that Allah showers His mercy upon you and grants you paradise. Finally, to my friends who have stood by me, understanding the demands of this journey and offering their unwavering support – you have been my pillars of strength. May Allah bless each one of you abundantly for your kindness and support. I am grateful to my colleagues, who have been like a second family with their camaraderie. Special thanks to my committee members for their feedback and valuable suggestions that have greatly enhanced my research. I also sincerely appreciate the School of Physics and N.O.R. lab staff's essential technical support and encouragement.

TABLE OF CONTENTS

ACKNOWLEDGEMENTS ..... **ii**

TABLE OF CONTENTS ..... **iii**

LIST OF TABLES ..... **vi**

LIST OF FIGURES ..... **xi**

LIST OF SYMBOLS ..... **xxii**

LIST OF ABBREVIATIONS ..... **xxv**

ABSTRAK ..... **xxvi**

ABSTRACT ..... **xxviii**

CHAPTER 1 INTRODUCTION **1**

1.1 Introduction 1

1.2 Problem Statement 3

1.3 Objectives 4

1.4 Originality of the Study 5

1.5 Scope of the Study 6

1.6 Outline of the Thesis 7

CHAPTER 2 BACKGROUND AND LITERATURE REVIEW **8**

2.1 Nanotechnology and Nanomaterials 8

2.2 Synthesis and Classification of Nanomaterials 9

2.3 Fundamentals of Metal Oxide Semiconductors 13

2.4 Overview of ZnO 16

2.5 UV Photodetectors 25

2.6 Impact of Doping on ZnO Synthesis, Applications, and UV Photodetector Efficiency 31

2.7 Laser Assisted Chemical Bath Deposition (LACBD) of ZnO NSs.....38

2.8 Mechanisms of Action.....43

CHAPTER 3 METHODOLOGY..... 64

3.1 Introduction.....64

3.2 Materials and Chemical Specifications.....64

3.3 Characterization and Equipment.....66

3.4 Precursor Solution Preparation.....66

3.5 Synthesis of ZnO Films and Substrate Selection.....67

3.6 Effects of Precursor on ZnO Films.....68

3.7 Analysis of the Effects of Laser Parameters.....70

3.8 Comparative Analysis of CBD versus LACBG.....70

3.9 Metal–Semiconductor–Metal (MSM) UV Photodetector.....72

3.10 Calculation and Analysis.....76

CHAPTER 4 INVESTIGATING THE EFFECTS OF PRECURSOR SELECTION AND LASER PARAMETERS ON THE MORPHOLOGICAL, STRUCTURAL, AND OPTICAL PROPERTIES OF ZNO FILMS..... 82

4.1 Introduction.....82

4.2 Influence of Substrates on ZnO Films.....83

4.3 Influence of Precursors on ZnO Films.....91

4.4 Influence of Laser Parameters.....130

4.5 Comparison Between CBD and LACBG.....157

4.6 Chapter Summary.....167

CHAPTER 5 ANALYSIS OF THE PHOTODETECTION PERFORMANCE IN UNDOPED AND DOPED ZNO-BASED UV PHOTODETECTORS..... 169

5.1 Introduction.....169

5.2 Influence of Various Metal Contacts on the Performance of ZnO Films-Based UV Photodetector.....170

5.3 Mg Doping Concentrations Impact on ZnO Film UV Photodetector 189

5.4 Cu Doping Concentrations Impact on ZnO Film UV Photodetector 205

5.5 Ag Doping Concentrations Impact on ZnO Film UV Photodetector 221

5.6 Mg/Cu Co-doping Concentrations Impact on ZnO Film UV Photodetector236

5.7 Ag/Cu Co-doping Concentrations Impact on ZnO Film UV Photodetector 251

5.8 Ag/Mg Co-doping Concentrations Impact on ZnO Film UV Photodetector 263

5.9 Ag/Mg/Cu Triple Doping Concentrations Impact on ZnO Film UV Photodetector.....275

5.10 Comparative Analysis of Metal-Doped ZnO Films in this Study.....289

5.11 Comparative Analysis of Metal-Doped ZnO Films with Other Studies 298

5.12 Chapter Summary.....308

CHAPTER 6 CONCLUSION AND FUTURE RECOMMENDATIONS.... 310

6.1 Conclusion.....310

6.2 Recommendations for Future Research 312

REFERENCES..... 315

LIST OF PUBLICATIONS

LIST OF TABLES

Page

Table 2.1 Advantages and limitations of some of the synthesis techniques. 10

Table 2.2 Influences of synthesis parameters on the properties of ZnO films. 22

Table 2.3 Literature review of the characteristics and optical properties of ZnO films. 24

Table 2.4 Potential factors that affect ZnO film UV Photodetector Performance. 30

Table 2.5 Effect of single metal doping on morphology, structure, and optical properties of ZnO. 32

Table 2.6 Effect of double metal doping on morphology, structure, and optical properties of ZnO. 34

Table 2.7 Effect of triple metal doping on morphology, structure, and optical properties of ZnO. 34

Table 2.8 Doping and ZnO UV photodetectors. 36

Table 2.9 Advantages and limitations of LACBD. 39

Table 2.10 Factors influencing ZnO film synthesis via LACBD. 41

Table 2.11 Effects of laser parameters on the morphology and optical properties of semiconductor materials. 42

Table 2.12 Comparison of laser-induced techniques for material processing on different substrates 43

Table 3.1 The purity and sources of the starting chemicals. 65

Table 4.1 EDX analysis of the ZnO films on the different substrates. 85

Table 4.2 Lattice parameters and structural properties of ZnO films with the highest diffraction intensity (002) on various substrates. 89

Table 4.3 Urbach, direct, and indirect bandgap energies of ZnO films on various substrates 91

Table 4.4 EDX analysis of the ZnO films synthesized using various Zn sources. 94

Table 4.5 Lattice parameters and structural properties of ZnO films with highest diffraction (002). 96

Table 4.6 Urbach, direct, and indirect bandgap energies of ZnO films synthesized using various Zn sources. 98

Table 4.7 EDX analysis of the ZnO films synthesized using various agent salt sources. 102

Table 4.8 Lattice parameters and structural properties of ZnO films with highest diffraction for different agent salt sources. 104

Table 4.9 Urbach, direct, and indirect bandgap energies of ZnO films synthesized using various agent salts. 106

Table 4.10 EDX analysis of the ZnO films at varying zinc nitrate hexahydrate to HMTA ratios. 113

Table 4.11 Lattice parameters and structural properties of ZnO films with peak diffraction across various zinc nitrate hexahydrate to HMTA concentrations. 116

Table 4.12 Urbach, direct, and indirect bandgap energies of ZnO films with varying source concentrations. 120

Table 4.13 EDX analysis of ZnO films across varying molarities. 124

Table 4.14 Lattice parameters and structural properties of ZnO films with highest diffraction across varying molarities. 127

Table 4.15 Urbach, direct, and indirect bandgap energies of ZnO films at various molarities. 130

Table 4.16 EDX analysis of the ZnO films synthesized at varying laser irradiation times. 135

Table 4.17 Lattice parameters and structural properties of ZnO films with highest diffraction (002). 138

Table 4.18 Urbach, direct, and indirect bandgap energies of ZnO films synthesized at varying laser irradiation times. 140

Table 4.19 EDX analysis of the ZnO films synthesized at various laser irradiation wavelengths. 143

Table 4.20 Lattice parameters and structural properties of ZnO films with highest diffraction by laser irradiation wavelength. 145

Table 4.21 Urbach, direct, and indirect bandgap energies of ZnO films synthesized at various laser irradiation wavelengths. 148

Table 4.22 EDX analysis of the ZnO films synthesized under varying laser irradiation powers. 152

Table 4.23 Lattice parameters and structural properties of ZnO films synthesized under varying laser irradiation powers. 154

Table 4.24 Urbach, direct and indirect bandgap energy ZnO films synthesized under varying laser irradiation powers. 157

Table 4.25 EDX analysis of the ZnO films synthesized using (a) CBD and (b) LACBG methods. 161

Table 4.26 Lattice parameters and structural properties of ZnO films synthesized via the two methods. 164

Table 4.27 Urbach, direct, and indirect bandgap energy ZnO films synthesized using (a) CBD and (b) LACBG methods. 167

Table 5.1 EDX analysis of as-grown ZnO films on glass with various metal contacts. 175

Table 5.2 Lattice parameters and structure properties of as-grown ZnO films on glass with various contacts at highest diffraction (002). 178

Table 5.3 Urbach, direct, and indirect bandgap energies of as-grown ZnO films on glass substrates with various metal contacts. 181

Table 5.4 Parameters of as-grown ZnO films UV photodetector devices. 189

Table 5.5 EDX analysis of $Mg_xZnO_{(100-x)}$ films. 194

Table 5.6 Lattice parameters and structure properties of $Mg_xZnO_{(100-x)}$ films at highest diffraction (002). 197

Table 5.7 Urbach, direct, and indirect bandgap energies of $Mg_xZnO_{(100-x)}$ films. 200

Table 5.8 Parameters of S41 UV photodetector device. 205

Table 5.9 EDX analysis of $Cu_xZnO_{(100-x)}$ films. 209

Table 5.10 Lattice parameters and structure properties of $Cu_xZnO_{(100-x)}$ films at highest diffraction (002). 211

Table 5.11 Urbach, direct, and indirect bandgap energies of $Cu_xZnO_{(100-x)}$ films. 214

Table 5.12 Parameters of S45 UV photodetector device. 220

Table 5.13 EDX analysis of $Ag_xZnO_{(100-x)}$ films. 224

Table 5.14 Lattice parameters and structure properties of $Ag_xZnO_{(100-x)}$ films at highest diffraction (002). 228

Table 5.15 Urbach, direct, and indirect bandgap energies of $Ag_xZnO_{(100-x)}$ films. 230

Table 5.16 Parameters of S49 UV photodetector device. 236

Table 5.17 EDX analysis of $Mg_xCu_xZnO_{(100-2x)}$ films 239

Table 5.18 Lattice parameters and structure properties of $Mg_xCu_xZnO_{(100-2x)}$ films at highest diffraction (002). 242

Table 5.19 Urbach, direct, and indirect bandgap energies of $Mg_xCu_xZnO_{(100-2x)}$ films. 245

Table 5.20 Parameters of S52 UV photodetector device. 251

Table 5.21 EDX analysis of $Ag_xCu_xZnO_{(100-2x)}$ films. 254

Table 5.22 Lattice parameters and structure properties of $Ag_xCu_xZnO_{(100-2x)}$ films at highest diffraction (002). 256

Table 5.23 Urbach, direct, and indirect bandgap energies of $Ag_xCu_xZnO_{(100-2x)}$ films. 258

Table 5.24 Parameters of S55 UV photodetector device. 262

Table 5.25 EDX analysis of $Ag_xMg_xZnO_{(100-2x)}$ films. 266

Table 5.26 Lattice parameters and structure properties of $Ag_xMg_xZnO_{(100-2x)}$ films at highest diffraction (002). 268

Table 5.27 Urbach, direct, and indirect bandgap energies of $Ag_xMg_xZnO_{(100-2x)}$ films. 270

Table 5.28 Parameters of S58 UV photodetector device. 275

Table 5.29 EDX analysis of $Ag_xMg_xCu_xZnO_{(100-3x)}$ films. 278

Table 5.30 Lattice parameters & structure properties of $Ag_xMg_xCu_xZnO_{(100-3x)}$ films - (100), (002), & (101) peaks. 280

Table 5.31 Urbach, direct, and indirect optical bandgap energy of $Ag_xMg_xCu_xZnO_{(100-3x)}$ films. 283

Table 5.32 Parameters of S60 UV photodetector device. 289

Table 5.33 Summary Comparison of Dopants Effect on ZnO Films. 291

Table 5.34 Comparison of UV photodetector performance of undoped samples with other studies. 299

Table 5.35 Comparison of SEM, XRD, UV-Vis results of single doped samples with other studies. 301

Table 5.36 Comparison of SEM, XRD, UV-Vis results of co-doped samples with other studies. 303

Table 5.37 Comparison of SEM, XRD, UV-Vis results of triple-doped samples with other studies. 305

Table 5.38 Comparison of UV photodetector performance of doped samples with other studies 307

LIST OF FIGURES

Page

Figure 1.1 Examples of the various applications of ZnO NSs. 3

Figure 2.1 An illustration of the different classifications of nanomaterials. 12

Figure 2.2 The classification of nanomaterial synthesis methodologies into bottom-up and top-down approaches. 13

Figure 2.3 An illustration of direct and indirect band gap semiconductors. 15

Figure 2.4 An illustration of the different ZnO crystal structures. 16

Figure 2.5 Schematic of energy levels of ZnO. 19

Figure 2.6 An illustration of Schottky contacts. 28

Figure 2.7 An illustration of ohmic contacts to an n-type semiconductor. 29

Figure 2.8 Energy bandgaps in (a) n-type and (b) p-type semiconductors.....31

Figure 2.9 Energy redistribution in interactions between lasers and materials involves (a) absorption, (b) diffusion, and (c) adjacent layers that absorb and diffuse. 48

Figure 2.10 Comparison of optical penetration depths of laser radiation of different wavelengths in a metal oxide film (≈1–10 μm thick). 52

Figure 2.11 (a) Specular reflection from a flat surface (b) Light capture by repeated reflections off rough surface structures. 56

Figure 2.12 Diagram of a ZnO film photodetector: (a) Oxygen adsorption creates a surface depletion zone, (b) UV light generates electron-hole pairs, (c) Recombination triggers oxygen desorption, (d) ZnO film under UV light, (e) Schottky barrier formation at the electrode interface. 59

Figure 3.1 An illustration of the precursor solution preparation procedure. 67

Figure 3.2 An illustration of the synthesis of ZnO films on various substrates. 68

Figure 3.3 Substrate preparation and solution parameters selection. 69

Figure 3.4 An illustration of the optimal laser parameters study. 71

Figure 3.5 MSM-UV photodetector fabrication. 73

Figure 3.6 An illustration of the doping process. 75

Figure 4.1 SEM images of ZnO films grown on the different substrates, (a) on glass, (b) on silicon, and (c) on PET. 84

Figure 4.2 EDX analysis of the ZnO films on the different substrates, (a) on glass, (b) on silicon, and (c) on PET. 85

Figure 4.3 XRD patterns of ZnO films grown on the different substrates, left—full 2θ scan ($20° \leq 2\theta \leq 80°$); right—zoomed view of the same patterns in the $30° \leq 2\theta \leq 40°$ range. 87

Figure 4.4 (a) UV-visible absorption spectrum, (b) Urbach energy, (c) Direct bandgap energy, and (d) Indirect bandgap energy of ZnO films on various substrates. 90

Figure 4.5 SEM images of ZnO films synthesized using various Zn sources, (a) Zinc nitrate hexahydrate, (b) Zinc acetate dihydrate, and (c) Zinc chloride. 93

Figure 4.6 EDX analysis of the ZnO films synthesized using various Zn sources, (a) Zinc nitrate hexahydrate, (b) Zinc acetate dihydrate, and (c) Zinc chloride. 94

Figure 4.7 XRD patterns of ZnO films synthesized using various Zn sources, left—full 2θ scan ($20° \leq 2\theta \leq 80°$); right—zoomed view of the same patterns in the $30° \leq 2\theta \leq 40°$ range. 95

Figure 4.8 (a) UV–visible absorption spectrum, (b) Urbach energy, (c) Direct bandgap energy, and (d) Indirect bandgap energy of ZnO films synthesized with different Zn sources. 97

Figure 4.9 SEM images of ZnO films synthesized using various agent salt sources, (a) HMTA, (b) KOH, and (c) NaOH. 100

Figure 4.10 EDX analysis of the ZnO films synthesized using various agent salt sources, (a) HMTA, (b) KOH, and (c) NaOH. 101

Figure 4.11 XRD patterns of ZnO films prepared from different agent salt sources, left—full 2θ scan ($20° \leq 2\theta \leq 80°$); right—zoomed view of the same patterns in the $30° \leq 2\theta \leq 40°$ range.....103

Figure 4.12 (a) UV–Visible absorption spectra, (b) Urbach energies, (c) Direct bandgap energies, and (d) Indirect bandgap energies of the ZnO films. 105

Figure 4.13 SEM images of ZnO films at varying zinc nitrate hexahydrate to HMTA ratios, (a) 1:4, (b) 2:4, (c) 3:4, (d) 4:4, (e) 4:3, (f) 4:2, (g) 4: 1, and (h) 4:0. 109

Figure 4.14 EDX analysis of the ZnO films at varying zinc nitrate hexahydrate to HMTA ratios, (a) 1:4, (b) 2:4, (c) 3:4, (d) 4:4, (e) 4:3, (f) 4:2, (g) 4: 1, and (h) 4:0. 111

Figure 4.15 XRD patterns of ZnO films at varying zinc nitrate hexahydrate to HMTA ratios, left—full 2θ scan ($20° \leq 2\theta \leq 80°$); right—zoomed view of the same patterns in the $30° \leq 2\theta \leq 40°$ range.....115

Figure 4.16 (a) UV-Visible absorption spectra, (b) Urbach energy, (c) direct bandgap, and (d) indirect bandgap of ZnO films with varying concentrations of zinc nitrate hexahydrate to HMTA.....118

Figure 4.17 SEM images of ZnO films at varying molarities, (a) 0.05 M, (b) 0.1 M, (c) 0.15 M, and (d) 0.2 M. 122

Figure 4.18 EDX analysis of ZnO films at varying molarities, (a) 0.05 M, (b) 0.1 M, (c) 0.15 M, and (d) 0.2 M. 123

Figure 4.19 XRD patterns of ZnO films at various molarities, left—full 2θ scan ($20° \leq 2\theta \leq 80°$); right—zoomed view of the same patterns in the $30° \leq 2\theta \leq 40°$ range.....126

Figure 4.20 (a) UV-Visible absorption spectrum, (b) Urbach energy, (c) Direct bandgap energy, and (d) Indirect bandgap energy of ZnO films at varying molarities.....129

Figure 4.21 SEM Images of ZnO films synthesized at various laser irradiation times with their cross-section, at (a) T = 4 min, (b) T = 6 min, (c) T = 8 min, and (d) T =10 min. 133

Figure 4.22 EDX analysis of ZnO films synthesized at varying laser irradiation times, at (a) T = 4 min, (b) T = 6 min, (c) T = 8 min, and (d) T =10 min. 134

Figure 4.23 XRD patterns of ZnO films synthesized at varying laser irradiation times, left—full 2θ scan ($20° \leq 2\theta \leq 80°$); right—zoomed view of the same patterns in the $30° \leq 2\theta \leq 40°$ range. 136

Figure 4.24 (a) UV–visible absorption spectrum, (b) Urbach energy, (c) Direct bandgap energy, and (d) Indirect bandgap energy of ZnO films. 139

Figure 4.25 SEM images of ZnO films at varying laser wavelengths with their cross-section, at (a) λ = 444.5 nm and (b) λ = 532 nm. 142

Figure 4.26 EDX analysis of the ZnO films synthesized at various laser irradiation wavelengths, at (a) λ = 444.5 nm and (b) λ = 532 nm....143

Figure 4.27 XRD patterns of ZnO films synthesized at various laser irradiation wavelengths, left—full 2θ scan ($20° \leq 2\theta \leq 80°$); right—zoomed view of the same patterns in the $30° \leq 2\theta \leq 40°$ range.....144

Figure 4.28 (a) UV–visible absorption spectrum, (b) Urbach energy, (c) Direct optical bandgap energy, and (d) Indirect optical bandgap energy of ZnO films. 147

Figure 4.29 SEM images of ZnO films synthesized under varying laser irradiation powers with their cross-section, at (a) P = 1 W, (b) P = 3 W, (c) P = 5 W, and (d) P = 7 W.....150

Figure 4.30 EDX analysis of the ZnO films synthesized under varying laser irradiation powers, at (a) P = 1 W, (b) P = 3 W, (c) P = 5 W, and (d) P = 7 W.....151

Figure 4.31 XRD patterns of ZnO films synthesized under varying laser irradiation powers, left—full 2θ scan ($20° \leq 2\theta \leq 80°$); right—zoomed view of the same patterns in the $30° \leq 2\theta \leq 40°$ range. 153

Figure 4.32 (a) UV–visible absorption spectrum, (b) Urbach energy, (c) Direct bandgap energy, and (d) Indirect bandgap energy of ZnO films. 156

Figure 4.33 SEM images of ZnO films synthesized using (a) CBD and (b) LACBG methods with their cross-section. 159

Figure 4.34 EDX analysis of the ZnO films synthesized using (a) CBD and (b) LACBG methods.....160

Figure 4.35 XRD patterns of ZnO films synthesized using (a) CBD and (b) LACBG methods, left—full 2θ scan ($20° \leq 2\theta \leq 80°$); right—zoomed view of the same patterns in the $30° \leq 2\theta \leq 40°$ range. 163

Figure 4.36 (a) UV-visible absorption spectrum, (b) Urbach energy, (c) Direct optical bandgap energy, and (d) Indirect optical bandgap energy. ..166

Figure 5.1 SEM of as-grown ZnO films on glass with various metal contacts, (a) Al, (b) Ni, (c) Ag, and (d) Cu. 173

Figure 5.2 EDX analysis of as-grown ZnO films on glass with various metal contacts, (a) Al, (b) Ni, (c) Ag, and (d) Cu. 174

Figure 5.3 XRD patterns of as-grown ZnO films on glass with various metal contacts, left—full 2θ scan ($20° \leq 2\theta \leq 80°$); right—zoomed view of the same patterns in the $30° \leq 2\theta \leq 40°$ range.....176

Figure 5.4 (a) UV–visible absorption spectrum, (b) Urbach energy, (c) Direct Bandgap Energy, and (d) Indirect Bandgap Energy of as-grown ZnO films on glass with various metal contacts. 179

Figure 5.5 I–V Characteristics of as-grown ZnO films for UV photodetector across various contacts, (a) Al, (b) Ni, (c) Ag, and (d) Cu. 184

Figure 5.6 Photocurrent response under 1 V bias with 2.0 mW/cm² pulsed light illumination: (a, b) at 365 nm wavelength for Al and Ni contacts; (c, d) at 385 nm wavelength for Ag and Cu contacts.....186

Figure 5.7 A single normalized photocurrent response cycle under 1V bias and 2.0 mW/cm² light intensity: (a, b) At 365 nm wavelength for Al and Ni contacts; (c, d) at 385 nm wavelength for Ag and Cu contacts.....188

Figure 5.8 SEM images of $Mg_xZnO_{(100-x)}$ films, (a) x = 0.5, (b) x = 1.0, (c) x =1.5, and (d) x = 2.0.....192

Figure 5.9 EDX spectra of $Mg_xZnO_{(100-x)}$ films, (a) x = 0.5, (b) x = 1.0, (c) x =1.5, and (d) x = 2.0. 193

Figure 5.10 XRD analysis of $Mg_xZnO_{(100-x)}$ films, left—full 2θ scan ($20° \leq 2\theta \leq 80°$); right—zoomed view of the same patterns in the $30° \leq 2\theta \leq 40°$ range. 195

Figure 5.11 (a) UV–visible absorption spectrum, (b) Urbach energy, (c) Direct optical bandgap, (d) Indirect optical bandgap of $Mg_xZnO_{(100-x)}$ films. 199

Figure 5.12 I–V characteristics of $Mg_xZnO_{(100-x)}$ films UV photodetectors under UV light (365 nm, 0.8 mW/cm²), (a) x = 0.5, (b) x = 1.0, (c) x =1.5, and (d) x = 2.0. 201

Figure 5.13 I–V characteristics of $Mg_xZnO_{(100-x)}$ films in S41 UV photodetector: (a) varying wavelengths at 0.8 mW/cm² intensity, (b) varying intensities at 385 nm wavelength. 202

Figure 5.14 Photocurrent response of S41 to pulsed UV light (385 nm, 2.0 mW/cm²) at varying bias voltages, (a) -1 V bias voltage, (b) -2 V bias voltage, and (c) -3 V bias voltage. 203

Figure 5.15 A single normalized photocurrent cycle response to UV light under various bias voltages of S41, (a) -1 V bias voltage, (b) -2 V bias voltage, and (c) -3 V bias voltage. 204

Figure 5.16 SEM of $Cu_xZnO_{(100-x)}$ films, (a) x = 0.5, (b) x = 1.0, (c) x =1.5, and (d) x = 2.0. 207

Figure 5.17 EDX spectra of $Cu_xZnO_{(100-x)}$ films, (a) x = 0.5, (b) x = 1.0, (c) x =1.5, and (d) x = 2.0. 208

Figure 5.18 XRD of $Cu_xZnO_{(100-x)}$ films, left—full 2θ scan ($20° \leq 2\theta \leq 80°$); right—zoomed view of the same patterns in the $30° \leq 2\theta \leq 40°$ range. 210

Figure 5.19 (a) UV-Visible Optical absorption spectrum, (b) Urbach energy, (c) Direct optical bandgap Energy, and (d) Indirect optical bandgap Energy of $Cu_xZnO_{(100-x)}$ films. 213

Figure 5.20 I–V characteristics of $Cu_xZnO_{(100-x)}$ films UV photodetectors under UV light (365 nm, 0.8 mW/cm²), (a) x = 0.5, (b) x = 1.0, (c) x =1.5, and (d) x = 2.0. 216

Figure 5.21 I–V characteristics of S4 UV photodetector of S45: (a) varying wavelengths at 0.8 mW/cm² intensity, (b) varying intensities at 385 nm wavelength. 217

Figure 5.22 Photocurrent response under pulsed UV light (385 nm, 2.0 mW/cm²) at different bias voltages for S45, (a) -1 V bias voltage, (b) -2 V bias voltage, and (c) -3 V bias voltage. 218

Figure 5.23 A single normalized photocurrent response cycle under various bias voltages in S45 with UV illumination, (a) -1 V bias voltage, (b) -2 V bias voltage, and (c) -3 V bias voltage. 219

Figure 5.24 SEM of $Ag_xZnO_{(100-x)}$ films, (a) x = 0.5, (b) x = 1.0, (c) x =1.5, and (d) x = 2.0. 222

Figure 5.25 EDX spectra of $Ag_xZnO_{(100-x)}$ films, (a) x = 0.5, (b) x = 1.0, (c) x =1.5, and (d) x = 2.0. 223

Figure 5.26 XRD patterns for $Ag_xZnO_{(100-x)}$ films, left—full 2θ scan ($20° \leq 2\theta \leq 80°$); right—zoomed view of the same patterns in the $30° \leq 2\theta \leq 40°$ range. 226

Figure 5.27 (a) UV–vis absorption spectrum, (b) Urbach energy, (c, d) direct and indirect optical bandgap energies of $Ag_xZnO_{(100-x)}$ films. 229

Figure 5.28. I–V characteristics of $Ag_xZnO_{(100-x)}$ films UV photodetectors under UV light (365 nm, 0.8 mW/cm²), (a) x = 0.5, (b) x = 1.0, (c) x =1.5, and (d) x = 2.0. 232

Figure 5.29 I–V Characteristics of S49 (a) varying wavelengths at 0.8 mW/cm² intensity, (b) varying intensities at 385 nm wavelength. 233

Figure 5.30 Photocurrent Response to Pulsed Light and Bias Voltage in S49 under UV Illumination (385 nm, 2.0 mW/cm²), (a) -1 V bias voltage, (b) -2 V bias voltage, and (c) -3 V bias voltage. 234

Figure 5.31 A single normalized photocurrent cycle of S49 under varied bias voltage and UV illumination, (a) -1 V bias voltage, (b) -2 V bias voltage, and (c) -3 V bias voltage. 235

Figure 5.32 SEM of $Mg_xCu_xZnO_{(100-2x)}$ films, (a) x = 0.5, (b) x = 1.0, and (c) x =1.5. 238

Figure 5.33 EDX spectra of $Mg_xCu_xZnO_{(100-2x)}$ films, (a) x = 0.5, (b) x = 1.0, and (c) x =1.5. 239

Figure 5.34 XRD analysis of $Mg_xCu_xZnO_{(100-2x)}$ films, left—full 2θ scan ($20° \leq 2\theta \leq 80°$); right—zoomed view of the same patterns in the $30° \leq 2\theta \leq 40°$ range. 241

Figure 5.35 (a) UV–visible absorption, (b) Urbach energy, (c) Direct bandgap, and (d) Indirect bandgap of $Mg_xCu_xZnO_{(100-2x)}$ films. 244

Figure 5.36 I–V characteristics of $Mg_xCu_xZnO_{(100-2x)}$ films UV photodetectors under UV light (365 nm, 0.8 mW/cm²), (a) x = 0.5, (b) x = 1.0, and (c) x =1.5. 246

Figure 5.37 I–V characteristics of $Mg_xCu_xZnO_{(100-2x)}$ films for UV photodetector of S3: (a) varying wavelengths at 0.8 mW/cm² intensity, (b) varying intensities at 395 nm wavelength. 247

Figure 5.38 Photocurrent response to pulsed light illumination at varying bias voltage for S52 under UV light exposure (395 nm, 2.0 mW/cm^2), (a) -1 V bias voltage, (b) -2 V bias voltage, and (c) -3 V bias voltage. 249

Figure 5.39 A single normalized photocurrent cycle under varying bias voltage for S52 under UV illumination, (a) -1 V bias voltage, (b) -2 V bias voltage, and (c) -3 V bias voltage. 250

Figure 5.40 SEM for $Ag_xCu_xZnO_{(100-2x)}$ films, (a) x = 0.5, (b) x = 1.0, and (c) x =1.5. 252

Figure 5.41 EDX spectra of $Ag_xCu_xZnO_{(100-2x)}$ films, (a) x = 0.5, (b) x = 1.0, and (c) x =1.5. 253

Figure 5.42 XRD analysis of $Ag_xCu_xZnO_{(100-2x)}$ films, left—full 2θ scan ($20° \leq 2\theta \leq 80°$); right—zoomed view of the same patterns in the $30° \leq 2\theta \leq 40°$ range. 255

Figure 5.43 (a) UV-vis absorption spectrum, (b) Urbach energy, (c) Direct optical bandgap, and (d) Indirect optical bandgap of $Ag_xCu_xZnO_{(100-2x)}$ films.....257

Figure 5.44 I–V characteristics of $Ag_xCu_xZnO_{(100-2x)}$ films UV photodetectors under UV light (365 nm, 0.8 mW/cm²), (a) x = 0.5, (b) x = 1.0, and (c) x =1.5. 259

Figure 5.45 I-V characteristics of $Ag_xCu_xZnO_{(100-2x)}$ films in UV photodetector of S55: (a) Different wavelengths, constant intensity (0.8 mW/cm²); (b) Different intensities, constant wavelength (λ = 365 nm). 260

Figure 5.46 Photocurrent response under pulsed light and UV (365 nm, 2.0 mW/cm²) at different bias voltages for S55, (a) -1 V bias voltage, (b) -2 V bias voltage, and (c) -3 V bias voltage. 261

Figure 5.47 A single normalized photocurrent cycle under varying S55 bias voltage and UV illumination, (a) -1 V bias voltage, (b) -2 V bias voltage, and (c) -3 V bias voltage. 262

Figure 5.48 SEM for $Ag_xMg_xZnO_{(100-2x)}$ films, (a) x = 0.5, (b) x = 1.0, and (c) x =1.5. 264

Figure 5.49 EDX spectra of $Ag_xMg_xZnO_{(100-2x)}$ films, (a) x = 0.5, (b) x = 1.0, and (c) x =1.5. 265

Figure 5.50 XRD analysis of $Ag_xMg_xZnO_{(100-2x)}$ films, left—full 2θ scan ($20° \leq 2\theta \leq 80°$); right—zoomed view of the same patterns in the $30° \leq 2\theta \leq 40°$ range. 267

Figure 5.51 (a) UV-visible absorption spectrum, (b) Urbach energy, (c,d) direct and indirect optical bandgaps of $Ag_xMg_xZnO_{(100-2x)}$ films. 269

Figure 5.52 I–V characteristics of $Ag_xMg_xZnO_{(100-2x)}$ films UV photodetectors under UV light (365 nm, 0.8 mW/cm²), (a) x = 0.5, (b) x = 1.0, and (c) x =1.5. 271

Figure 5.53 I-V characteristics of S3 film in UV photodetector of S58: (a) varying wavelengths at 0.8 mW/cm² intensity, (b) varying intensities at 365 nm wavelength. 272

Figure 5.54 Photocurrent response under pulsed light illumination at various bias voltages for S58 with UV exposure (365 nm, 2.0 mW/cm²), (a) -1 V bias voltage, (b) -2 V bias voltage, and (c) -3 V bias voltage. 273

Figure 5.55 A single normalized photocurrent cycle under varying bias voltage for S58 device under UV exposure, (a) -1 V bias voltage, (b) -2 V bias voltage, and (c) -3 V bias voltage. 274

Figure 5.56 SEM for $Ag_xMg_xCu_xZnO_{(100-3x)}$ films, (a) x = 0.5 and (b) x = 1.0. .277

Figure 5.57 EDX Spectra of $Ag_xMg_xCu_xZnO_{(100-2x)}$ films, (a) x = 0.5 and (b) x = 1.0. 278

Figure 5.58 XRD analysis of $Ag_xMg_xCu_xZnO_{(100-3x)}$ films, left—full 2θ scan ($20° \leq 2\theta \leq 80°$); right—zoomed view of the same patterns in the $30° \leq 2\theta \leq 40°$ range. 279

Figure 5.59 (a) UV–visible optical absorption spectrum, (b) Urbach energy, (c) Direct optical bandgap, and (d) Indirect optical bandgap of $Ag_xMg_xCu_xZnO_{(100-3x)}$ films. 282

Figure 5.60 I–V characteristics of $Ag_xMg_xCu_xZnO_{(100-3x)}$ films UV photodetectors under UV light (365 nm, 0.8 mW/cm²), (a) x = 0.5 and (b) x = 1.0. 285

Figure 5.61 I-V Characteristics of $Ag_xMg_xCu_xZnO_{(100-3x)}$ films UV photodetectors of S60 at: (a) Varying wavelengths, 0.8 mW/cm², (b) Varying intensities, 385 nm. 286

Figure 5.62 Photocurrent response to pulsed light under varied bias voltage for S60, with UV illumination (365 nm, 2.0 mW/cm^2), (a) -1 V bias voltage, (b) -2 V bias voltage, and (c) -3 V bias voltage. 287

Figure 5.63 A single normalized photocurrent cycle of S60 under varying bias voltage with UV illumination, (a) -1 V bias voltage, (b) -2 V bias voltage, and (c) -3 V bias voltage. 288

Figure 5.64 Comparative analysis of direct optical bandgap energies in (a) Metal-doped and (b) Metal-co-doped ZnO semiconductors. 292

Figure 5.65 Comparative analysis of rise and decay times in UV photodetectors with metal-doped ZnO films at varying reverse bias voltages.....293

Figure 5.66 Comparative analysis of dark and photocurrents in UV photodetectors with metal-doped ZnO films under varying reverse bias voltages. 295

Figure 5.67 Comparison of UV photodetectors with metal-doped ZnO films under reverse bias voltage: (a) Responsivities, (b) Quantum Efficiencies, (c) Sensitivities, (d) Gains, (e) Detectivities, (f) Noise Equivalent Powers.....297

LIST OF SYMBOLS

A	Area
A/W	Ampere per Watt
Ag	Silver (chemical element)
Å	Angstrom (10^{-10} m)
a, b, c	Lattice parameters
c	Speed of light
cm	Centimetre
Cu	Copper (chemical element)
D	Crystallite size
d	Interplanar spacing
D_s	Specific detectivity
E	Photon energy
E_g	Band-gap energy
e	Elementary charge
eV	Electron volt
G	Current gain
h	Planck's constant
hv	Photon energy
Hz	Hertz
I	Current
I_d	Dark current
I_{ph}	Photocurrent
KOH	Potassium hydroxide (chemical formula)
L	Zn–O bond length (wurtzite)

M	Molarity (mol L^{-1})
mA	Milliampere
Mg	Magnesium (chemical element)
ms	Millisecond
mW/cm^2	Milliwatts per square centimetre
N	Number of crystallites per unit volume
$NaOH$	Sodium hydroxide
nm	Nanometre
P	Power
R	Responsivity
Si	Silicon (chemical element)
T	Time
V	Volume / Voltage (context-dependent)
$ZnCl_2$	Zinc chloride
ZnO	Zinc oxide
$°C$	Degrees Celsius
μA	Microampere
α	Absorption coefficient
β	Full width at half maximum
γ	Decay constant / Absorptivity
δ	Dislocation density
ε	Micro-strain
η	Quantum efficiency
θ	Angle in XRD
λ	Wavelength
μ	Positional parameter
ν	Frequency of light

ρ	Lattice strain
σ	Stress
τ_d	Decay time
τ_r	Rise time

LIST OF ABBREVIATIONS

AC	Alternating Current
at%	Atomic Percent
CBD	Chemical Bath Deposition
Cu Kα	Copper K-alpha radiation
DC	Direct Current
EDX	Energy-Dispersive X-ray Spectroscopy
EQE	External Quantum Efficiency
FESEM	Field-Emission Scanning Electron Microscopy
FWHM	Full Width at Half Maximum
G	Glass (substrate)
HMTA	Hexamethylenetetramine
II-IV	Periodic-table group numbers for Zn & O
IV or I-V	Current-Voltage characteristics
LACBD	LaserAssisted Chemical Bath Deposition
LACBG	Laser-Assisted Chemical Bath Growth
LED	Light-Emitting Diode
MSM	Metal-Semiconductor-Metal configuration
NEP	Noise-Equivalent Power
NSs	Nanostructures
OLED	Organic Light-Emitting Diode
PET	Polyethylene Terephthalate
SEM	Scanning Electron Microscopy
TFs	Thin Films
UV	Ultraviolet
UV-Vis	Ultraviolet-Visible Spectroscopy
wt%	Weight Percent
XRD	X-ray Diffraction

TEKNIK PERTUMBUHAN RENDAMAN KIMIA BERBANTU LASER UNTUK KOMPOSIT ZINK OKSIDA BAGI PENINGKATAN PRESTASI FOTOPENGESAN UV

ABSTRAK

Optoelektronik telah maju dengan bahan semikonduktor seperti filem zink oksida (ZnO) yang didop dengan logam, yang meningkatkan kecekapan peranti UV kerana jalur tenaga yang lebar dan tenaga pengikatan eksiton yang tinggi. Mensintesis bahan-bahan ini merupakan cabaran, memerlukan teknik yang kompleks. Kajian ini menggunakan kaedah Pertumbuhan Mandian Kimia Berbantu Laser (LACBG), satu teknik yang cekap dan mesra alam, untuk memperbaiki struktur nano ZnO bagi meningkatkan kecekapan fotodetektor UV. Kajian ini meneroka tahap pendopan daripada tanpa dop hingga didop dengan tiga logam, menilai pengaruhnya terhadap prestasi fotodetektor, dengan tumpuan kepada pengoptimuman sintesis dan kesan pendopan terhadap sifat ZnO dan pengesanan UV. Proses ini bermula dengan membersihkan substrat—kaca, silikon, dan PET—memilih pelbagai garam (sumber zink dan agen), dan menyesuaikan kepekatan dan molariti untuk mengoptimumkan pembentukan ZnO. Parameter laser (masa penyinaran, panjang gelombang, kuasa) dikaji untuk memperbaiki sintesis. Pencirian melibatkan SEM, EDX, XRD, dan spektroskopi UV-Visible untuk menganalisis morfologi, komposisi, struktur, dan sifat optik, yang kemudian dibandingkan dengan teknik Pemendapan Mandian Kimia (CBD). Akhirnya, fotodetektor UV-MSM difabrikasi dan diuji di bawah cahaya UV. Keadaan optimum dicapai menggunakan $Zn(NO_3)_2 \cdot {}_6H_2O$ dan $C_6H_{12}N_4$ pada substrat

kaca dengan nisbah kepekatan 1:1 dan molariti 0.10 M, di bawah panjang gelombang 445.5 nm dan laser 5 W selama 6 minit. Pendopan tiga logam menunjukkan prestasi unggul, dengan $Ag_xMg_xCu_xZnO_{(100-3x)}$ sebagai kombinasi pendopan dua logam terbaik dan $Ag_xZnO_{(100-x)}$ sebagai pendopan tunggal terbaik. Ag mengungguli Cu dalam kalangan bahan kontak. Analisis jalur tenaga menunjukkan peralihan biru untuk pendopan Mg tunggal (3.24 hingga 3.67 eV) dan peralihan merah untuk pendopan Cu dan Ag (3.35 hingga 2.96 eV dan 3.28 hingga 2.84 eV, masing-masing); pendopan dua logam dengan $Ag_xMg_xZnO_{(100-2x)}$ menyebabkan peralihan biru (3.4 hingga 3.5 eV), manakala semua sampel pendopan tiga logam menunjukkan peralihan merah (3.12 hingga 2.81 eV). Kristalografi menunjukkan orientasi pada paksi c (satah 002) untuk semua sampel kecuali sampel yang didop tiga logam, yang lebih cnderung pada satah 101. Pendopan tiga logam pada x= 1.0 at% untuk setiap logam menunjukkan sifat elektrik yang luar biasa, termasuk nadi segi empat dengan masa naik (22.69 ms) dan masa reput yang rendah (26.18 ms), kepekaan tinggi (20954.85), responsiviti (24.95 A/W), detektif (5.29×10^7 Jones), penguatan (210.55), dan kecekapan (84.67%), dengan kuasa bersamaan bunyi yang rendah (2.27×10^{-11}) pada bias -3 V, di bawah cahaya UV 365 nm dan intensiti 2.0 mW/cm^2. Teknik LACBG menawarkan kaedah yang cekap, mesra alam, dan kos efektif untuk mensintesis ZnO films bagi fotodetektor UV. Dengan mengoptimumkan keadaan sintesis dan menggabungkan pendopan logam, proses LACBG mengatasi kaedah CBD konvensional, terutamanya dengan ZnO films yang didop tiga logam yang mempamerkan sifat unggul.

LASER ASSISTED CHEMICAL BATH GROWTH TECHNIQUE OF ZINC OXIDE COMPOSITE FOR ENHANCED UV PHOTODETECTOR PERFORMANCE

ABSTRACT

This study uses the Laser Assisted Chemical Bath Growth (LACBG) method, an efficient, eco-friendly technique, to improve zinc oxide (ZnO) films for enhanced UV photodetector efficiency. It explores doping levels from undoped to triple-metal-doped, assessing their influence on photodetector performance, with a focus on synthesis optimization and the effects of doping on ZnO properties and UV detection. The process started with cleaning substrates—glass, silicon, and PET—selecting various salts (zinc and agent sources), and adjusting concentrations and molarity to optimize ZnO formation. Laser parameters (irradiation time, wavelength, power) were studied to refine synthesis. Characterization involved SEM, EDX, XRD, and UV-Visible spectroscopy to analyze morphology, composition, structure, and optical properties, which were then compared with the Chemical Bath Deposition (CBD) technique. Finally, MSM-UV photodetectors were fabricated and tested under UV light. Optimal conditions were achieved using $Zn(NO_3)_2{\cdot}_6H_2O$ and $C_6H_{12}N_4$ on a glass substrate at a 1:1concentration ratio and 0.10 M molarity, under 445.5 nm wavelength and 5 W laser for 6 minutes. Ag outperformed Cu among contact materials. Bandgap analysis indicated a blue shift for single Mg doping (3.24 to 3.67 eV) and red shifts for Cu and Ag doping (3.35 to 2.96 eV and 3.28 to 2.84 eV, respectively); double doping with $Ag_xMg_xZnO_{(100-2x)}$ caused a blue shift (3.4 to 3.5 eV), while all triple doping samples exhibited red shifts (3.12 to 2.81 eV). Crystallography showed orientation at the c-axis (002 plane) for all except triple-doped samples, which preferred the (101

plane). Triple doping at $x =$ 1.0 at% for each metal exhibited exceptional electrical properties, including a rectangular pulse with low rise (22.69 ms) and decay times (26.18 ms), high sensitivity (20954.85), responsivity (24.95 A/W), detectivity (5.29×10^7 Jones), gain (210.55), and efficiency (84.67%), with low noise equivalent power (2.27×10^{-11}) at a -3 V bias, under 365 nm UV light and 2.0 mW/cm^2 intensity. LACBG provides a rapid, green route to doped ZnO films, and optimized metal triple-doped ZnO UV photodetectors with markedly improved speed and sensitivity.

CHAPTER 1 INTRODUCTION

1.1 Introduction

Optoelectronics have advanced rapidly through the use of semiconductors such as zinc oxide (ZnO) films, which combine a wide bandgap (~3.37 eV) with a high exciton binding energy (~60 meV) to enable efficient UV emission, detection and light harvesting [88]. Owing to its biocompatibility and stability, ZnO finds application in UV LEDs, photodetectors, gas sensors and solar cells, and—as a photocatalyst—supports pollutant degradation; it also sees use in cosmetics and textiles for UV-blocking and antimicrobial coatings [291, 302].

ZnO can be synthesized through various techniques, each suitable for specific applications and desired properties. One common method is the sol-gel process, which involves the hydrolysis and polycondensation of zinc salts to form a gel-like network that converts into ZnO upon drying and thermal treatment. Another popular technique is vapor deposition, including chemical vapor deposition (CVD) and physical vapor deposition (PVD), which are ideal for producing high-purity and uniformly thin ZnO films used in electronics and optics. Additionally, the hydrothermal method, where aqueous solutions of zinc salts are reacted under high temperature and pressure, is widely used for scalable production of ZnO nanoparticles with excellent control over particle size and shape [40, 114, 242].

Generally, doping ZnO with metals such as aluminum, gold, silver, and nickel enhances its ultraviolet (UV) photoluminescence, allowing the development of UV optoelectronic devices [378]. Additionally, ZnO's ability to form different nanostructures, such as nanowires and nanorods, allows researchers to explore excitonic emissions and develop devices like UV nanolasers and photodetectors [215, 217]. UV photodetectors exploit wide bandgap semiconductors to detect high-energy UV

photons, converting them into electronic signals. These devices are crucial for applications like gas sensing and flame detection due to their high stability, sensitivity, and selectivity [231, 420]. The metal-semiconductor-metal (MSM) design is predominant, often incorporating nanostructured semiconductors to improve responsivity and photocurrent gains, due to their large surface-to-volume ratios [320, 403]. ZnO-based detectors are particularly notable for their robustness and enhanced sensitivity through mechanisms like oxygen adsorption-desorption and metal doping, which boost electron-hole pair production [41, 281, 417]. Additionally, semiconductor contacts play a significant role, with Schottky and ohmic contacts formed based on doping levels and work functions, influencing the charge transport and overall performance of the photodetectors [408].

ZnO nanostructurs are also used due to their large exciton binding energy, which proves especially useful for lasing actions that depend on exciton recombination [54]. Furthermore, these materials have been utilized in energy storage [290]. However, the complexity of doping processes, especially with multiple metals, presents challenges and offers opportunities to customize ZnO's properties for specific needs. Various studies have shown that understanding the interactions between dopants and their effects on ZnO’s optoelectronic properties is important for optimizing device performance [199, 445] (Figure 1.1).

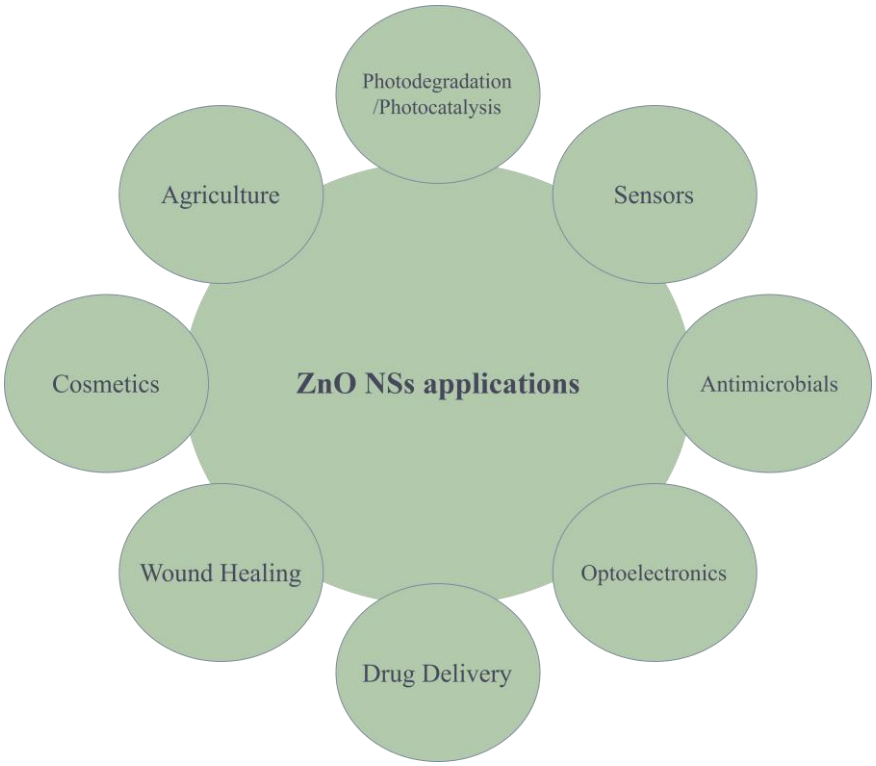

Figure 1.1 Examples of the various applications of ZnO NSs.

1.2 Problem Statement

ZnO is a promising semiconductor for ultraviolet (UV) photodetection due to its wide bandgap and high exciton binding energy [369]. However, conventional synthesis techniques often lead to non-uniform nanostructures with significant defects and impurities, resulting in reduced device performance and reliability [253]. Moreover, many of these methods are costly, involve complex equipment setups, and are difficult to scale for large-volume production [278]. Consequently, ZnO-based UV photodetectors frequently exhibit low sensitivity, slow response times, and high dark current [214]. They can also suffer from poor stability under prolonged UV exposure, partly due to insufficient crystallinity and the lack of a controllable bandgap tailored for selective UV detection [345].

These limitations highlight an urgent need for a robust, cost-effective, and easily scalable fabrication approach that can produce high-quality ZnO nanostructures.

Additionally, methods to enhance device performance—such as reducing defects, improving crystallinity, and stabilizing the wurtzite structure—are critical to achieving faster response times, lower dark current, and better long-term stability [350]. Metal doping has shown promise for increasing localized surface plasmon resonances, enabling bandgap engineering, and improving photoconductive gain; however, integrating such dopants in a controlled, reproducible way remains a challenge [104].

This research addresses these gaps by proposing a Laser-Assisted Chemical Bath Growth (LACBG) technique to synthesize both doped and undoped ZnO films for UV photodetector fabrication. The LACBG process offers precise control over growth parameters, enabling uniform and defect-free ZnO films even at reduced temperatures and pressures, which can help lower production costs and simplify scale-up. The strategic incorporation of metallic dopants is further leveraged to tailor the bandgap, enhance structural stability, suppress dark current, and improve the overall sensitivity and speed of the resulting UV photodetectors.

1.3 Objectives

The overarching objective of this study is to utilize and refine the LACBG technique for the synthesis of a variety of ZnO films, including undoped, single, double, and triple metal-doped, and to evaluate their effectiveness in UV photodetector applications, specifically:

1. To optimize the synthesis conditions of the precursor solution and the LACBG technique by adjusting various parameters including zinc salt source, agent salt source, concentration, molarity, as well as fine-tuning the laser irradiation time, wavelength, and power involved in the synthesis processes

2. To investigate the effects of doping—single, double, and triple—by analyzing the integration of various dopants—Silver (Ag), Copper (Cu), and Magnesium (Mg)—within the ZnO lattice and its impact on the performance of UV photodetectors.
3. To evaluate the effect of different metal contacts, wavelength and intensity of incident light, and bias voltage on the performance of ZnO UV photodetectors.

1.4 Originality of the Study

This research introduces a LACBG technique for synthesizing single-, double-, and triple-doped ZnO films, offering precise reaction control to enhance film quality, purity, scalability, and cost-effectiveness. By integrating various metallic dopants, the study strategically exploits localized surface plasmon resonances, reduces carrier recombination, and traps charge carriers in engineered defect states, thereby lowering dark current and stabilizing the wurtzite structure for heightened UV responsiveness.

Moreover, bandgap tuning is achieved to optimize UV detection while suppressing visible-light interference, ensuring improved photoconductive gain and long-term stability. This technique also promotes greener synthesis processes and accommodates adjustable laser parameters, enabling researchers to fine-tune material properties in a flexible, scalable manner. Taken together, these contributions position LACBG as a transformative approach for high-performance ZnO-based UV photodetectors, bridging the gap between laboratory innovation and industrial-scale production.

1.5 Scope of the Study

To achieve the objectives of this study, its scope is limited to:

1. Examining the synthesis of ZnO films using various precursors, concentrations, and molarities, in addition to analyzing their impacts on surface morphology, crystal structure, and optical properties.
2. Optimize the LACBG technique for synthesizing ZnO films by adjusting laser parameters (laser irradiation time, wavelength, and power) and studying their effects on film properties. Then, the optimized LACBG technique will be compared with chemical bath deposition (CBD) to evaluate their respective advantages and limitations.
3. Assessing how different types of metal contact (electrodes) affect the performance of ZnO UV photodetectors. This involves testing various metals to see how they influence the photodetectors' efficiency, responsiveness, and overall functionality.
4. Exploring the doping of ZnO films with different elements (Ag, Cu, Mg) and their combinations to observe how single, double, and triple doping can modify ZnO's electronic and optical properties. The integration of these dopants into the ZnO lattice and their impact on UV photodetector performance will be a key focus.
5. Investigating how the bias voltage, alongside the wavelength and intensity of incident light, affects the performance of the UV photodetectors. This will help understand the photodetectors' dynamic responses under various operational conditions and optimize them for better performance.

1.6 Outline of the Thesis

The thesis is divided into six chapters, beginning with Chapter 1: Introduction to Laser Assisted ZnO Film Synthesis for UV Photodetector, problem statement, objectives, the scope of the study, the originality, and thesis outline

Chapter 2: "Background and Literature Review," reviews the basics of ZnO films, touching on their characteristics, uses, and the progression of synthesis methods up to recent advancements.

Chapter 3: "Methodology" describes the research's technical setup, detailing the creation processes, doping approaches, and analysis instruments.

Chapter 4: "Investigating the Effects of Precursor Selection and Laser Parameters on the Morphological, Crystalline, and Optical Properties of ZnO films" highlighting noticeable changes or trends in their morphology, crystallinity, and optical behavior.

Chapter 5: "Analysis of the Photodetection Performance in Undoped and Doped ZnO films-based UV Photodetectors" explores the development and examination of the UV photodetector, concentrating on the performance analysis of the various doped samples.

Chapter 6: "Conclusions and Future Directions" concludes the study, summarizing its key findings and significance and suggesting avenues for further inquiry based on the research results.

CHAPTER 2 BACKGROUND AND LITERATURE REVIEW

2.1 Nanotechnology and Nanomaterials

Nanotechnology has impacted the development of functional materials and devices; this encompasses various fields, including optoelectronics, solar cells, and photocatalysis [240]. This technology leverages the distinct properties of materials at the nanoscale to achieve performance characteristics unattainable by their bulk counterparts. Accordingly, nanomaterials, characterized by their dimensions being 1 to 100 nanometers in at least one dimension, have emerged as key components in engineering advanced UV photodetectors [73, 450].

The origin of nanotechnology is often traced back to the pioneering work of Michael Faraday in the synthesis of colloidal gold nanoparticles in 1857. However, it was not until the late 20th century, following Richard Feynman's visionary lecture "There is Plenty of Room at the Bottom" and the advent of the scanning tunneling microscope, that nanotechnology emerged as a distinct field. This period marked the beginning of rapid developments in synthesizing and applying various nanomaterials, including nanoparticles, nanotubes, and quantum dots, each characterized by distinct physical, chemical, and electrical properties due to their nanoscale dimensions [30, 378, 441].

This diversity in nanomaterials has been necessary in developing and enhancing UV photodetectors, which influence nanomaterials' unique optical and electronic properties to offer superior performance over traditional materials [273]. The application of nanotechnology in this field has led to significant advancements, with nanomaterials enabling the development of more sensitive UV photodetectors, have faster response times, and are capable of operating over a broader spectrum of UV light, thereby finding critical applications in environmental monitoring, communication

technologies, and healthcare [30, 221, 404]. Integrating nanotechnology with semiconductor science has opened new avenues for developing advanced UV photodetectors, facilitating the exploration of novel materials and device architectures that promise even greater efficiencies and functionalities [267].

Advances in nanotechnology research throughout the years have been substantial, with innovations in nanofabrication techniques allowing for the precise manipulation of nanomaterials to enhance UV photodetector device performance [26, 207, 441]. Despite these advancements, the development and application of nanotechnology confront several challenges. Technical difficulties in manufacturing at the nanoscale, such as ensuring consistency, scalability, and cost-effectiveness, remain barriers. Moreover, nanomaterials' health and environmental impacts necessitate thorough investigation to address these concerns [136, 223].

2.2 Synthesis and Classification of Nanomaterials

Advancements in nanotechnology have significantly enhanced the ability to manipulate and synthesize semiconductor nanostructures with precision that approaches the atomic level [83]. This advancement is fundamental in developing nanostructures such as quantum wells, wires, and dots, which exhibit electronic state densities distinct from those predicted by conventional quantum mechanical models [135]. The synthesis of these nanostructures utilizes sophisticated techniques, including chemical vapor deposition, physical vapor deposition, electrospinning, sol-gel, pulse laser-assisted chemical bath deposition, and laser-induced hydrothermal growth [26, 115, 441]. These methods enable the controlled fabrication of nanostructures, tailoring their electronic, optical, and mechanical properties to suit specific applications, from optoelectronics to

catalysis [312, 441, 445]. Table 2.1 outlines the advantages and potential limitations of commonly used synthesis techniques.

Table 2.1 Advantages and limitations of some of the synthesis techniques.

Method	Advantages	Potential Limitations	Ref.
Sol-Gel Process	Low-temperature processing, reasonable control over stoichiometry, and uniformity	It requires curing and post-treatment and may have cracks or defects in films.	[40, 75]
Atomic Layer Deposition (ALD)	Excellent control over film thickness, conformal coatings	Slow deposition rates, limited to surface reactions	[169, 242]
Hydrothermal Synthesis	Low temperature, environmentally friendly, good crystallinity	Limited to materials stable at high pressures and temperatures	[114, 428]
Chemical Vapor Deposition (CVD)	Can produce high purity, high-performance films, versatile	Requires high temperatures, potentially hazardous precursor handling	[242]
Physical Vapor Deposition (PVD)	Good control over film thickness and composition, clean process	Line-of-sight deposition limits the coating of complex shapes	[149]
Spray Pyrolysis	Simple and scalable, suitable for large areas	Difficult to control stoichiometry and uniformity	[149, 284, 318]
Microwave-Assisted Synthesis	Rapid heating, reduces reaction times, energy efficient	Scalability issues and uneven heating can be a problem	[140]
Chemical Bath Deposition	Simple and inexpensive, good for large-area TFs	Difficult to control film thickness and homogeneity	[84]
Laser Induced Hydrothermal Growth	Precise control overgrowth, localized heating	Equipment intensive, limited to small areas	[110, 189]
Pulse Laser-Assisted Chemical Bath Deposition	Enhanced reaction rates, better control over deposition	Complex setups	[115]
Laser Assisted Chemical Bath Deposition	Good control over film properties, enhanced reaction rates	Necessitates advanced proficiency	[441]

The classification of nanomaterials into zero-dimensional (0D), one-dimensional (1D), two-dimensional (2D), and three-dimensional (3D) categories is based on their spatial confinement and dimensional properties, which fundamentally influence their quantum behavior and, consequently, their physical properties [450]. 0D structures, such as quantum dots and nanoparticles, confine electrons in all three spatial dimensions, leading to discrete energy levels and a delta-like density of states. These properties are exploited in applications requiring quantum confinement effects, including quantum dot solar cells and fluorescent markers in biological imaging [243, 317].

1D structures—like nanowires, nanorods, and nanotubes—permit electron mobility along a single axis, enhancing charge carrier mobility. This directional freedom results in a modified electronic state density advantageous for nanoscale electronic devices and sensors [402]. 2D structures like nanosheets and nanowalls, where electrons can move in two dimensions, exhibit high surface area and exceptional electrical properties, finding uses in flexible electronics, energy storage technologies, and photodetectors [139].

Three-dimensional structures, including nanoflowers and complex shapes like nano-tetrapods, combine bulk material properties with nanoscale surface effects. These structures are essential for applications with desirable macroscopic volume and high surface reactivity. The quantum effects that dominate the behavior of these materials lead to a density of states markedly different from that of bulk materials [383] (Figure 2.1).

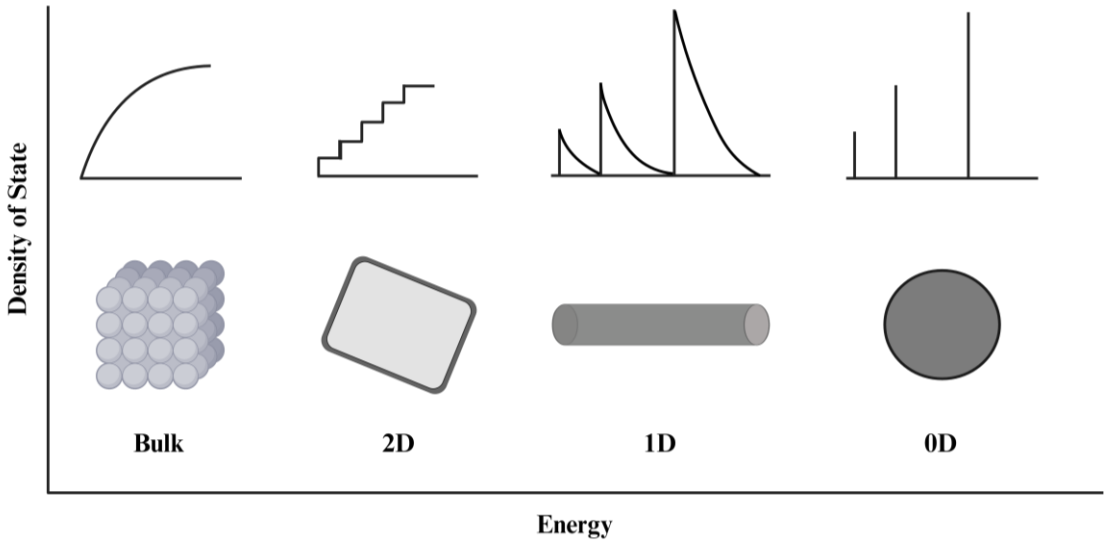

Figure 2.1 An illustration of the different classifications of nanomaterials.

Research in nanotechnology is often aimed at understanding the control over particle size, shape, and composition through various methods. The synthesis of nanomaterials is broadly categorized into two distinct methodologies: the bottom-up and top-down approaches [200].

The bottom-up approach, also known as the assembly approach, is characterized by the assembly of nanomaterials from the atomic or molecular scale. This method relies on the principle of self-assembly, where atoms or molecules spontaneously organize into structured nanomaterials under specific conditions. Techniques such as CVD, sol-gel processing, and molecular beam epitaxy exemplify the bottom-up strategy. The bottom-up approach is advantageous for creating nanomaterials with complex architectures, including quantum dots, nanowires, and layered structures. However, these techniques often encounter challenges such as controlling the assembly process and ensuring production scalability [200].

Conversely, the top-down approach involves the synthesis of nanomaterials from larger bulk materials through physical or mechanical means. This approach uses

advanced lithographic techniques, such as electron beam lithography and focused ion beam milling, to etch or mill materials down to the nanoscale. While this method offers advantages in terms of direct patterning and integration with existing manufacturing processes, it often faces limitations related to introducing defects (like doping), imperfections, and limitations in the complexity of the structures that can be achieved [200]. These methodologies are illustrated in Figure 2.2.

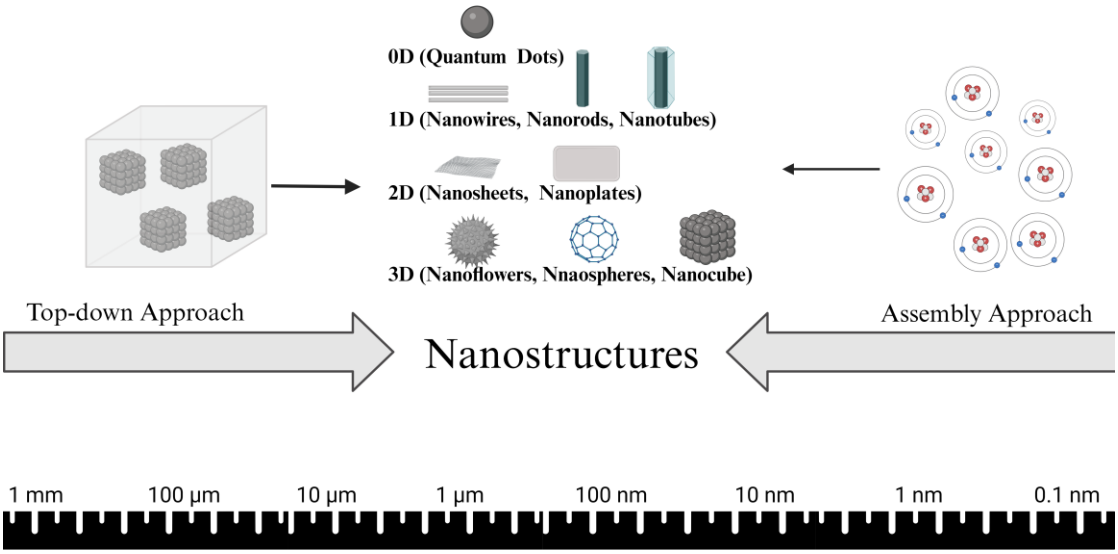

Figure 2.2 The classification of nanomaterial synthesis methodologies into bottom-up and top-down approaches.

2.3 Fundamentals of Metal Oxide Semiconductors

Metal oxide semiconductors (MOS) exhibit superior stability and reproducibility over organic counterparts in sensor applications, offering high sensitivity, affordability, simple fabrication, low energy consumption, high thermal resistance, catalytic capability, and efficient sensing mechanisms [324]. Additionally, due to their significant electrical attributes, MOS TFs are being investigated for potential in biosensors and memory devices [309, 324].

The importance of materials with high surface area-to-volume ratios in sensor technology cannot be overstated for their role in detecting minimal concentrations of analytes [163]. The selection of transistor and electrode configurations in electronic sensors is oftentimes critical, influencing sensitivity and facilitating active matrix functionality [211, 388]. MOS's compatibility with diverse analytes, chemical durability, high field-effect mobility, and manufacturing simplicity make them promising for biosensor development [419, 420].

The appeal of MOS extends to their transparency, scalability, and process compatibility, comprising metal cations (e.g., Zn, Cu, Ni) and oxide anions, including ternary and quaternary compositions [39, 406]. With silicon-based transistors' scalability and cost challenges, metal oxide-based thin-film transistors emerge as compelling substitutes in flexible and stretchable electronics [59].

Semiconductors are categorized into direct and indirect band gap types [426]. Direct band gap semiconductors allow efficient electron-hole recombination due to the alignment of valence and conduction bands in momentum space [35]. Conversely, indirect band gap semiconductors lack this alignment, necessitating phonons for momentum conservation during recombination, which diminishes their optical efficiency due to rarer electron-phonon interactions [310]. This is illustrated in Figure 2.3.

The investigation of the direct bandgap in photodetectors plays a crucial role in assessing their optical properties, specifically the optical absorption edge and the generation efficiency of electron-hole pairs when subjected to UV light. These parameters are integral to understanding the operational effectiveness of photodetectors, as they directly impact the device's ability to convert light into electrical signals. Furthermore, the study of the indirect bandgap sheds light on the interactions involving

phonons and the subtler electronic transitions that, despite their lower likelihood, are significant in influencing the sensitivity and overall efficiency of UV photodetectors [37, 58].

On the other hand, the measurement of Urbach energy is critical in understanding the disorder within ZnO films, particularly when altered by doping and co-doping techniques. The introduction of dopants such as Mg, Cu, and Ag, either individually or in combinations, leads to structural changes in the lattice, creating defect states that markedly influence the optical properties of these films [241]. Urbach energy, which measures the width of the tail of localized states in the bandgap resulting from these disorders and defects, offers deep insights into the severity of these defects and their influence on the optical absorption characteristics. Through analyzing Urbach energy, correlations between structural modifications induced by doping and changes in optical properties can be established [153, 398].

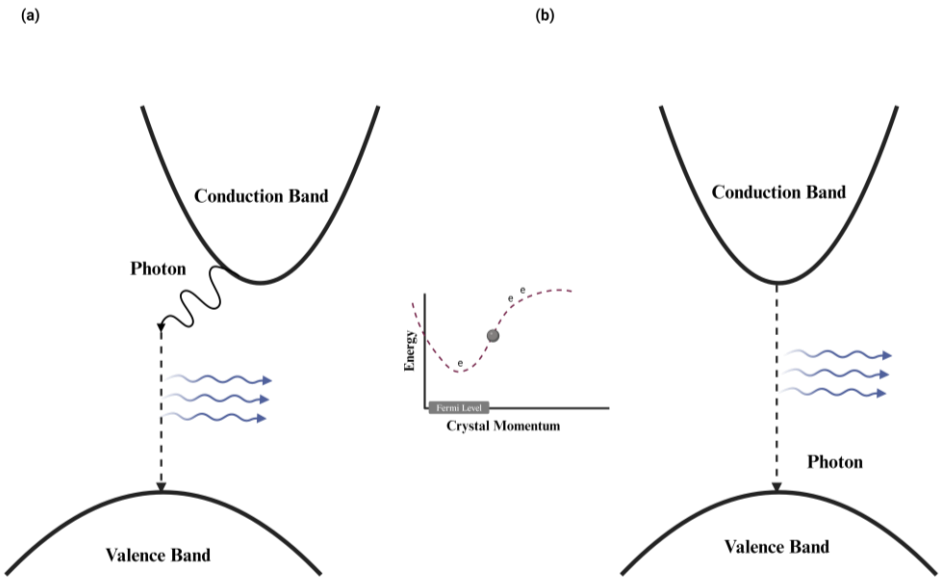

Figure 2.3 An illustration of direct and indirect band gap semiconductors.

2.4 Overview of ZnO

ZnO functions as an n-type semiconductor, characterized by a wide band gap of around 3.37 eV, and manifests in three crystalline forms: hexagonal wurtzite, cubic zinc blende, and cubic rock salt [270, 299] (Figure. 2.4). The hexagonal wurtzite structure is thermodynamically favored at ambient conditions, while zinc blende is only stable on cubic substrates [81]. Under high pressures, wurtzite transitions irreversibly to rock salt at room temperature, reverting to wurtzite only under elevated temperatures [205]. Wurtzite belongs to the space group C_{6v}^4, with lattice constants $a = b = 3.249$ Å, $c = 5.207$ Å, and interaxial angles $\alpha = \beta = 90°$, $\gamma = 120°$. In this configuration, zinc atoms are tetrahedrally bonded to four oxygen atoms, resulting in a hexagonal close-packed structure. The ionic radii are 0.74 Å for Zn^{2+} and 1.24 Å for O^{2-} [296].

ZnO exhibits alignment of its valence and conduction bands at a singular point within the Brillouin zone [158, 162]. Due to crystal field and spin-orbit interactions, the valence band undergoes splitting into three sub-bands. Additionally, understanding the variation of ZnO's band gap with temperatures up to 300 K is essential for evaluating its functional attributes [373].

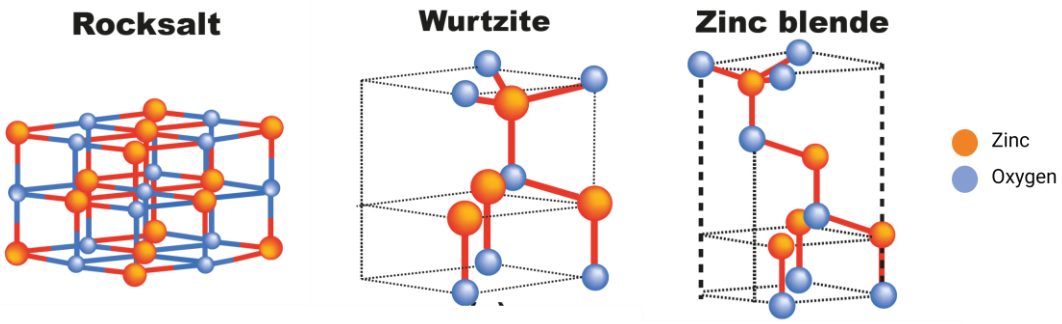

Figure 2.4 An illustration of the different ZnO crystal structures.

2.4.1 Electrical Characteristics of ZnO

Undoped ZnO inherently exhibits n-type conductivity, which is attributed to intrinsic defects such as oxygen vacancies and zinc interstitials [298]. As a direct, wide band gap semiconductor with a significant exciton binding energy (60 meV at room temperature), ZnO is advantageous for diverse electronic and optoelectronic uses [291]. Its wide band gap offers high breakdown voltages, low noise levels, and the capability to handle large electric fields, ensuring operability at elevated temperatures and power settings [266].

Electron dynamics within ZnO vary with electric field intensity. Under low electric fields, electrons experience minimal energy gains, maintaining a stable energy distribution and constant electron mobility per Ohm's law. Conversely, high electric fields give electrons substantial energy, generating "hot electrons" with temperatures surpassing the lattice's, achieving drift velocities beyond steady-state values [19].

The electrical characteristics of ZnO differ notably, especially concerning carrier concentration in n-type ZnO, which is influenced by the deposition method [423]. At room temperature, low-doped n-type ZnO demonstrates an electron mobility of approximately 200 $cm^2\ V^{-1}\ s^{-1}$ [269]. Although p-type doping in ZnO has been reported, further confirmation is required [44, 262].

2.4.2 Piezoelectric Attributes of ZnO

Wurtzite ZnO NSs exhibit notable piezoelectric properties. This is essential for their electromechanical response to applied mechanical stress and strain [122]. Strain describes the deformation of solids under external forces, whereas stress denotes the internal forces counteracting deformation [256]. Piezoelectricity in materials like ZnO

originates from atomic-level polarization changes induced by deformation. This phenomenon in ZnO can be ascribed to the tetrahedral coordination of oxygen and zinc atoms; external forces lead to a displacement of charge centers, thereby generating local dipole moments [68].

Uniform crystal orientations facilitate the manifestation of macroscopic dipole moments under applied forces or pressures. ZnO's piezoelectricity is further enhanced by its structure, featuring alternating layers of Zn^{2+} and O^{2-} atoms and the absence of a center of symmetry, endowing it with pronounced piezoelectric properties and substantial electromechanical coupling potential. These characteristics are invaluable for developing nano-electromechanical systems, sensors, and transducers with electromechanical coupling [248, 399].

2.4.3 Optical Behavior of ZnO

ZnO's direct wide band gap contributes to its optical properties, with emissions in the 400-600 nm range arising from both intrinsic and extrinsic defects—oxygen vacancies, interstitial oxygen, zinc vacancies, interstitial zinc, and defects—are integral to ZnO's performance [22, 177]. Investigations into ZnO's optical attributes reveal its utility in optoelectronics, with studies at room temperature demonstrating UV emission alongside defect-related visible emissions [179].

Changes influence ZnO's optical and electrical properties in the deep-level defects within its crystal structure. Figure 2.5 details ZnO's electronic structure, showing the conduction band (CB) and valence band (VB) along with intermediate energy states such as the free exciton, donor and acceptor bound excitons, and intrinsic defects Zn_i and Zn_V, marked by horizontal red lines. Transition energies between these

states and the bands include ≈ 3.37 eV for the free exciton to CB and 3.358 eV and 3.365 eV for the transitions from Zn_V and Zn_i defects to the VB, respectively [339] (Figure 2.5).

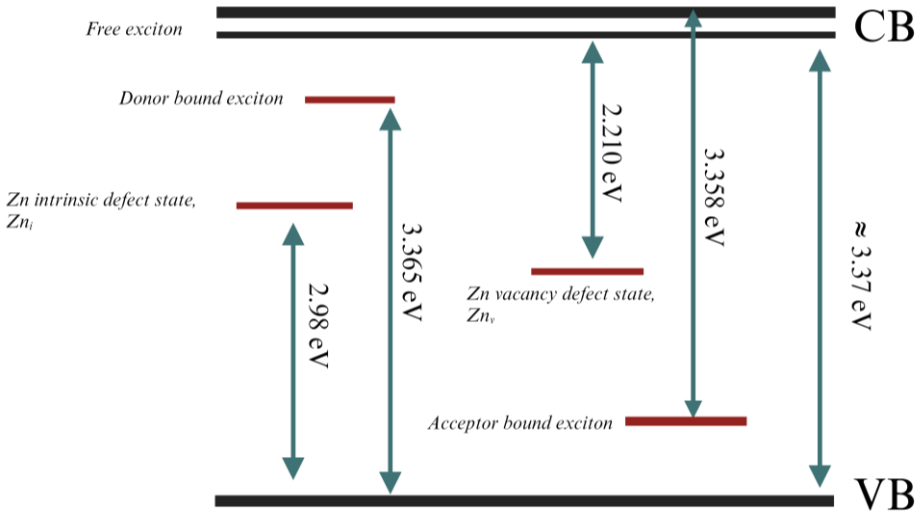

Figure 2.5 Schematic of energy levels of ZnO.

2.4.4 Background on ZnO's Direct Bandgap, Indirect Transitions, and Urbach Energy

ZnO is widely recognized as a direct wide-bandgap semiconductor, exhibiting a room-temperature bandgap of approximately 3.37 eV and a high exciton binding energy of about 60 meV [7]. In a direct-bandgap semiconductor, electrons can transition from the valence band to the conduction band (and vice versa) without requiring a change in momentum, which facilitates stronger optical absorption and emission processes. This characteristic makes ZnO a highly appealing material for optoelectronic devices, particularly in the ultraviolet (UV) range [17].

Despite being classified mainly as a direct-bandgap material, certain conditions, such as heavy doping, structural defects, or lattice distortions, can lead to the appearance

of indirect-like transitions in ZnO. In these cases, additional phonon interactions (lattice vibrations) assist the electron transitions between bands [282]. Such indirect transitions often manifest as broadened or lower-intensity peaks in optical absorption and photoluminescence spectra. The presence of these transitions can impact device performance, either by expanding the absorption range or introducing unwanted parasitic absorption and scattering losses [11]. Recognizing and controlling the balance between direct and any emerging indirect transitions are therefore pivotal in designing ZnO-based UV detectors and light-emitting devices.

Another important parameter in describing the absorption edge of ZnO is the Urbach energy. The Urbach energy characterizes the exponential tail of localized states extending into the bandgap, often referred to as the Urbach tail [124]. This tail is attributed to various disorder effects, such as defects, impurities, and other structural inhomogeneities within the crystal lattice [451]. A higher Urbach energy typically indicates increased disorder, which can adversely affect optical and electrical properties by introducing sub-bandgap absorption and diminishing carrier lifetimes. By contrast, a lower Urbach energy signifies a sharper absorption edge, reflecting a more ordered crystalline structure [124]. Minimizing disorder and hence the Urbach energy is key to maximizing the efficiency of ZnO-based UV photodetectors.

2.4.5 Thermal Properties of ZnO

ZnO in its wurtzite structure displays thermal characteristics that are essential for high-power and high-temperature device applications [99]. One key parameter is its thermal conductivity, which is significantly influenced by phonon-phonon scattering from inherent defects, dopant atoms, and other crystalline imperfections [452]. Defect

management, therefore, becomes pivotal: it can either enhance or impede phonon transport depending on the type, density, and distribution of these defects.

Another crucial property is thermal expansion, reflecting how the lattice dimensions change with temperature. Because wurtzite ZnO is anisotropic, its expansion coefficients along the a- and c-axes can differ, affecting stress and reliability in device structures. Also important is the specific heat capacity, which stems from contributions by lattice vibrations, charge carriers, and structural anomalies, and can vary widely based on doping level and crystal quality [155].

Furthermore, ZnO's volumetric heat capacity (approximately 2900 $kJ \cdot m^{-3}K^{-1}$) underscores its ability to absorb thermal energy, while its elastic constants (e.g., $E_{11} \approx 210$ GPa, $E_{33} \approx 211$ GPa) illustrate its robust mechanical stability. The average speed of sound in ZnO—ranging from about 2760 $m \cdot s^{-1}$ (transverse) to 6090 $m \cdot s^{-1}$ (longitudinal), further highlights the significance of phonon propagation for heat transfer. Meanwhile, a phonon frequency gap of around 3.98 THz emphasizes how lattice vibrations are quantized and can influence phonon scattering and thus thermal conductivity [400].

Taken together, these thermal properties need to be carefully managed in high-power or high-temperature ZnO-based devices, especially when doping strategies are introduced. By optimizing crystal quality, controlling defect concentrations, and fine-tuning doping protocols, ZnO can be tailored for reliable operation in thermally demanding environments.

2.4.6 Synthesis Parameters and Their Impact on ZnO Properties

Various factors significantly influence the properties of ZnO films during their fabrication. These factors include the choice of substrate, type of zinc salt source, and

doping agents, all of which affect the growth orientations, morphologies, and optical properties of ZnO films [361]. This includes electrical resistivity, growth orientation, and optical band gaps. Furthermore, the molarity and the molar concentration of Zn^{2+} ions also have an impact [4, 13, 157] (Table 2.2).

Table 2.2 Influences of synthesis parameters on the properties of ZnO films.

Factor		**Observed Changes in ZnO**	**Ref.**
Substrate	Glass	Granular and rough surface morphology; High transparency with an adjustable bandgap.	[287, 319, 361]
	Silicon	Uniform and dense layer; Compatible with semiconductor processes; Good epitaxial alignment for electronic applications.	
	PET	Improve ZnO seed adhesion, impacts nanorod morphology and density.	
Zinc Salt	Zinc acetate	Larger crystallites and nanoflakes. Reduces the optical band gap.	[16, 125, 326]
	Zinc nitrate	Increase grain size; shift the optical absorption band; enhance crystallinity and optical characteristics.	
	Zinc chloride	Enlarges crystallite size; changes morphology from nanorods to aggregated structures; varies the band gap energy.	
Agent Source	NaOH	Affects structure, wettability, and band gaps.	[4]
	KOH	Causes variations in cavity size, crystallinity, grain size, and band gap energy.	
	HMTA	Enhances the uniformity and smoothness; maintains hexagonal structure without forming secondary phases; increases the optical band gap energy,	
Molarity		Significantly impacts the electrical, morphological, structural, and optical properties, influencing factors like electrical resistivity, growth orientation, and optical band gaps.	[157]
Concentration		Impacts surface morphology, crystal orientation, and photocatalytic activity. These changes affect the optical band gap and UV light performance, influencing optical and photocatalytic properties.	[13, 157]

Research shows various synthesis conditions and their outcomes on ZnO films. For instance, using zinc acetate dehydrate with monoethanolamine in a 1:1 molar ratio results in a granular surface and a polycrystalline structure with a specific hexagonal bandgap [313]. In contrast, under certain conditions, zinc chloride forms rod-like structures with low transmittance and distinct optical properties[23]. Variations in the precursor concentration, such as those seen with zinc nitrate or zinc acetate combined

with different solvents, lead to diverse morphologies and structural adjustments, which influence the films' optical band gaps [6, 352] (Table 2.3).

In recent research, the growth conditions of ZnO films have been precisely manipulated using a selection of salts—specifically NaOH, KOH, and hexamethylenetetramine (HMTA). These salts play a crucial role in modulating both the pH and the ionic environment of the precursor solutions, significantly impacting ion dissociation processes vital for the formation of ZnO nanocrystals. The strong bases, NaOH and KOH, notably increase the solution's pH, enhancing the deprotonation of water and elevating OH^- ion concentrations, essential for ZnO formation through the hydrolysis and subsequent dehydration of zincite ($Zn(OH)_2$) into ZnO [1, 13, 14].

Conversely, HMTA functions as a buffer, controlling the release of formaldehyde and ammonia during decomposition, which in turn influences the crystallization process and the resultant morphology of the ZnO nanostructures. These variations in ionic concentrations and environmental pH, introduced by the different salts, have a marked influence on the nucleation and growth kinetics of the films, further affecting their optical and electrical properties which are crucial for enhancing their performance in UV photodetection applications [174, 201, 358].

Table 2.3 Literature review of the characteristics and optical properties of ZnO films.

Source of Zn Salt	Agent Salt Source	Conc.	Molarity	Surface Morphology	Crystal Structure	Optical Characteristics	Ref.
Zinc acetate dihydrate	C_2H_7NO	Variable	1:1 molar ratio	Granular surface	Hexagonal polycrystalline structure	Approximate bandgap of 3.25 eV	[313]
Zinc acetate	C_2H_6O & NH_4OH	-	-	Surface resembling grains, transparency over 75%	Polycrystalline with a hexagonal wurtzite structure	Bandgap energy ranging from 3.15 eV to 3.25 eV	[349]
Zinc chloride	-	-	0.1 M	Rod-like structures observed	Hexagonal phase, with (0 0 2) preferred orientation	Low light transmittance, bandgap approx. 3.30 eV	[23]
Zinc nitrate	$C_2H_8N_2$ & NaOH	-	ZnCl2 (0.04 M) and NaOH (0.08 M)	Varies based on precursors	Hexagonal wurtzite structure	Bandgap between 3.29 eV and 3.57 eV	[367]
Zinc acetate	$C_3H_8O_2$ & C_2H_7NO	0.15, 0.25, 0.5 M	Varies	Formation of nanofibers at higher concentrations	Good crystallinity at high concentrations	Bandgap narrows (3.28 eV to 3.22 eV) as concentration increases	[352]
Zinc acetate	$C_3H_8O_2$ & C_2H_7NO	0.15, 0.25, 0.5 M	Varies	Effects on dielectric constants, Urbach energy, and absorption.	-	Optical band gap varies with precursor concentration	[6]
Zinc chloride	NaOH	Variable	1 M to 0.01 M	Plate and powder-like morphology	-	Band gap ranges from 2.59 to 3.57 eV	[367]
Zinc acetate	$C_3H_8O_2$ & C_2H_7NO	-	0.075 to 0.175 M	Crystallite size and morphology dependent on zinc ion concentration	Hexagonal crystal structure with wurtzite symmetry	Low absorption at 340-999 nm, the band gap increases with zinc concentration to 3.8 eV	[157]